

Computational modelling of bone growth and mineralization surrounding biodegradable Mg-based and permanent Ti implants

Domenik Priebe^{*,1}, Nik Pohl^{*,1}, Tamadur AlBaraghteh^{1,2}, Sven Schimek¹, Florian Wieland¹,
Diana Krüger¹, Sascha Trostorff³, Regine Willumeit-Römer^{1,4},
Ralf Köhl^{3,4}, Berit Zeller-Plumhoff^{**,1,4,5}

*these authors have contributed equally to the manuscript

**corresponding author: berit.zeller-plumhoff@hereon.de, berit.zeller-plumhoff@uni-rostock.de

¹ Institute of Metallic Biomaterials, Helmholtz-Zentrum Hereon, Germany

² Institute of Surface Science, Helmholtz-Zentrum Hereon, Germany

³ Department of Mathematics, Faculty of Mathematics and Natural Sciences, Kiel University, Germany

⁴ Kiel, Nano, Surface, and Interface Science - KiNSIS, Kiel University, Germany

⁵ Data-driven Analysis and Design of Materials, Faculty of Mechanical Engineering and Marine Technologies,
University of Rostock, Germany

Abstract

In silico testing of implant materials is a research area of high interest, as cost- and labour-intensive experiments may be omitted. However, assessing the tissue-material interaction mathematically and computationally can be very complex, in particular when functional, such as biodegradable, implant materials are investigated. In this work, we expand and refine suitable existing mathematical models of bone growth and magnesium-based implant degradation based on ordinary differential equations. We show that we can simulate the implant degradation, as well as the osseointegration in terms of relative bone volume fraction and changes in bone ultrastructure when applying the model to experimental data from titanium and magnesium-gadolinium implants for healing times up to 32 weeks. By conducting a parameter study we further show that a lack of data at early time points has little influence on the simulation outcome. Moreover, we show that the model is predictive in terms of relative bone volume fraction with mean absolute errors below 6%.

1 Introduction

The development of biodegradable implant materials to support bone healing temporarily is a highly active area of research with many advances in the experimental field. Magnesium (Mg)-based alloys have already been introduced to the market with first CE-certifications issued. Further developments are ongoing in optimizing degradation rates, mechanical properties and the tissue response [1, 2]. It is increasingly acknowledged that mathematical and computational models yield significant potential to accelerate the experimental work, if predictive models can be achieved and implemented for *in silico* experiments. However, such models will often result in high complexities, due to the large number of cell processes involved in bone healing and remodelling [3] and their interactions with the changing chemical environment during implant degradation. Therefore, simplified models that simulate the mechanistic behaviour of peri-implant bone remodelling and implant degradation are desired.

Previously, a number of models of bone healing and remodelling, and Mg alloy degradation have been introduced, see reviews by Carlier et al. [4], Wang et al. [5], Oughmar et al. [6], and AlBaraghteh et al. [7]. Many of

these models are complex and defined using partial differential equations (PDEs) to incorporate spatial variations and dependencies. By contrast, Komarova et al. [8] introduced a model of bone mineralization depending on inhibitors, nucleators for mineralization, and the formation of mature collagen matrices using ordinary differential equations (ODEs). The authors apply their model to pathologies in which bone mineralization is perturbed, including osteogenesis imperfecta, and are able to show the model’s effectiveness in capturing main differences in the behaviour of the inhibitors and nucleators in these pathologies.

In the case of modelling Mg degradation, a number of simplified models have been introduced. Grogan et al. [9] introduced an expression of the mass loss rate based on the diffusivity of Mg^{2+} ions in the immersion medium and the saturation concentration of the ions therein. This simplified expression was able to yield results similar to a more complex PDE-based model. Recently, Gießgen et al. [10] presented a formulation of the degradation rate depending on the surface reaction rate and a parameter quantifying the amount of precipitated degradation product which hinders the degradation process. The authors highlight the improved performance of their model in capturing the experimentally observed degradation kinetics.

In the current work, we aim to use the model introduced by Komarova et al. [8] to describe the bone remodelling process surrounding different implant types, specifically magnesium-gadolinium (Mg-xGd) and titanium (Ti) implants. We further extend the model by incorporating the effect of Mg alloy degradation on the bone remodelling process. Finally, we include details on the mineralization process, namely the individual hydroxyapatite crystal growth and the influence of the different implant types thereon. To model the degradation process we implement the existing models by Grogan et al. [9] and Gießgen et al. [10]. In doing so, we evaluate how modelling the degradation kinetics influences on the bone remodelling kinetics. The models are calibrated against data from experiments for which implant volume loss V_{loss} , peri-implant bone volume fraction BV/TV , and bone crystal lattice spacing L and crystal width C_{width} were quantified. Importantly, the experiments to which we apply the models are those in which holes have been introduced into bone by drilling and an implant is then inserted using either a screw or a press fit.

2 Mathematical formulation of models

The ODE system used to describe Mg alloy degradation, bone growth and mineralization is derived in the following. A short explanation into the existence of solutions and their uniqueness is given in appendix A.

2.1 Modelling Mg alloy degradation

The mathematical descriptions for the volume loss rate $\frac{dV_{loss}}{dt}$ are taken from the literature. The diffusion-based power law introduced by Grogan et al. [9] for the mass loss rate is given as:

$$\frac{dM}{dt} = \frac{\alpha D^\beta c_{sat}}{\sqrt{t}},$$

where D is the diffusion coefficient of Mg^{2+} ions in the body fluid, c_{sat} their saturation concentration and $\alpha, \beta > 0$ are constant coefficients. At constant temperature D and c_{sat} are constant and due to the proportionality of mass and volume, we reformulate the equation to describe $\frac{dV_{loss}}{dt}$ by introducing m_1 :

$$\frac{dV_{loss}}{dt} = \frac{m_1}{\sqrt{t}} \tag{1\alpha}$$

The alternative description of volume loss is based on Gießgen et al. [10]. The authors introduced the

following equation to describe the degradation rate of a degradable metal:

$$\frac{dy_{corr}}{dt} = \frac{r \cdot d}{rt + d},$$

where y_{corr} is the average degradation depth given a surface degradation rate r and a parameter d that describes the influence of precipitated degradation products on the degradation process. The degradation rate is proportional to the volume loss rate by a factor V_0/A , where V_0 is the initial volume of the implant and A its surface area. Thus, the volume loss rate can be described as:

$$\frac{dV_{loss}}{dt} = \frac{A \cdot r \cdot d}{V_0(rt + d)} = \frac{r' d'}{r't + d'} \quad (1\beta)$$

for $r' = Ar/V_0$, $d' = Ad/V_0$.

2.2 Modelling peri-implant bone formation

The model of peri-implant bone growth and mineralization is based on the model presented by Komarova et al. [8]. We utilize the model formulation that was non-dimensionalized spatially and with respect to concentrations. Komarova et al. introduced their model of formation of mineralized bone based on the concept of bone tissue formation initiated by osteoblasts in the form of a naive collagen matrix x_1 . The matrix transforms into mature collagen matrix x_2 at a characteristic rate k_1 over time. This matrix will be mineralized as the amorphous hydroxyapatite located between the collagen fibres is taking crystalline form. This process is hindered by a combination of molecular inhibitors I which diffuse through the naive collagen matrix at a rate v_1 and are removed during matrix maturation at a rate r_1 so that the mineralization can occur. The mineralization of the hydroxyapatite begins at a number k_2 of nucleation sites N in the gaps between collagen fibres. These sites are created during matrix maturation. Any nucleation site that is enclosed in mineral H at a rate r_2 becomes inactive. The change in bone mineral depends on the inhibitors by means of a Hill function dependency, as well as the nucleation sites and a characteristic rate k_3 .

In applying this model to describe the formation of bone surrounding permanent implants made of Ti, we assume that the processes occur similarly and any specific influence of the implant is negligible and can be accounted for by the existing parameters. This is a reasonable assumption as the implant is fitted into a drilled hole and it is not degradable. Thus, new bone may be assumed to form based on the process described by the model. Moreover, we equate the amount of formed mineral concentration H to the amount of mineralized bone which is experimentally often quantified using the parameter of relative bone volume fraction BV/TV . We assume for our model that H and BV are proportional since the hydroxyapatite is assumed to grow homogeneously around the nucleators. Consequently, the amount of molecules may be assumed to be proportional to the volume in which they are growing, which again are homogeneously distributed in the bone volume and therefore the bone volume grows proportionally to the hydroxyapatite molecule number. Therefore, H and BV/TV are proportional to each other by further accounting for the constant total volume investigated. Thus, we may incorporate this proportionality constant in an updated parameter k'_3 .

In the case of Mg-based implants, the model additionally needs to account for the effect of the degradation of the implant. It has previously been shown Mg leads to a delay in hydroxyapatite formation [11]. Thus, the rate of release of Mg^{2+} ions, which can be assumed to be inverse to the rate of volume loss, influences the inhibitor concentration I at a rate m_2 . Thus, the formation of bone around Ti and Mg alloy implants can be described by the following system of ODEs. The term added in gray is that added to the model introduced by Komarova et al. [8] used only when describing bone formation around Mg alloys:

$$\frac{dx_1}{dt} = -k_1 x_1 \quad (1a)$$

$$\frac{dx_2}{dt} = k_1 x_1 \quad (1b)$$

$$\frac{dI}{dt} = v_1 x_1 - r_1 x_2 I + m_2 \frac{dV_{loss}}{dt} \quad (1c)$$

$$\frac{dN}{dt} = k_2 \frac{dx_2}{dt} - r_2 \frac{dH}{dt} N \quad (1d)$$

$$\frac{dH}{dt} = k_3 \cdot \frac{b}{b + (I)^a} \cdot N \quad (1e)$$

All parameters $k_1, v_1, r_1, m_2, k_2, r_2, k_3 \in \mathbb{R}_{>0}$. Because V_{loss} is a fraction, no non-dimensionalization is necessary.

2.3 Modelling bone mineral growth

To model the growth of the hydroxyapatite crystals in more detail as this relates to the mechanical properties of the bone [12] and include the effect of the released Mg^{2+} ions thereon, we further introduce models to describe the change in crystallite size and lattice spacing of the hydroxyapatite crystal over time.

To this end, we assume that the hydroxyapatite nucleates as thin layers within the gaps between collagen fibers [13]. Hydroxyapatite has a hexagonal shape and is assumed to grow first along its (002) plane before growing in width along the (310) plane [13]. Thus, initially, the hydroxyapatite crystal can be described by a needle-like structure that later expands into platelets [14]. Therefore, we assume a fixed crystal length, which has been shown to measure 30-50 nm [15]. In accordance with the information provided by Ostapienko et al. [16] for crystal growth, we model the change in crystal thickness C_{width} as a function depending on the difference in hydroxyapatite concentration on the existing crystal surface and surrounding body fluid:

$$\frac{dC_{width}}{dt} = K_c L_{SA} (c_0 - c^*)^g,$$

where K_c is the crystallization reaction constant, L_{SA} is the surface area of the crystal, c_0 is the solute concentration in the fluid, c^* is the equilibrium concentration and g represents the order of the crystal growth process. As the crystal is assumed to grow over time, L_{SA} cannot be considered constant and should be approximated.

The surface area of an individual hydroxyapatite crystal needle/platelet is difficult to determine, therefore, we assume that the crystal geometry can be represented by a prism with a regular n -sided base, where $n > 3$. Thus, we may approximate both the needle-like and platelet forms effectively. The following expression can be derived for the surface area, the derivation of which is given in appendix B:

$$L_{SA} = k_{10} \cdot C_{width},$$

with a proportionality constant $k_{10} \in \mathbb{R}_{>0}$.

The difference between the equilibrium concentration and the body fluid, $(c_0 - c^*)$, drives the crystal growth in this model. Hydroxyapatite precipitates if $(c_0 - c^*) > 0$ [16] and would therefore increase H . Thus, the change in bone mineral content $\frac{dH}{dt}$ relates to these concentrations by some rate constant k_5 : $(c_0 - c^*) = k_5 \frac{dH}{dt}$. If $(c_0 - c^*) = 0$, then $\frac{dH}{dt} = 0$. With $k_4 := K_c \cdot k_{10}$ and $k_6 := g$, the change in crystal width C_{width} over time is described as:

$$\frac{dC_{width}}{dt} = k_4 \cdot C_{width} \cdot \left(k_5 \cdot \frac{dH}{dt}\right)^{k_6}.$$

Finally, we aim to include the influence of Mg^{2+} ion release on the crystal lattice spacing. This parameter is generally fixed for a bone with some spatial variations depending on health, age, etc. However, if certain ions are present in bone at sufficient concentrations, they may be incorporated into the crystal lattice by replacing Ca^{2+} ions, thus changing the crystal lattice spacing due to a difference in atomic radius [17, 18].

Currently, no model has been published that considers a change in crystal lattice spacing due to a replacement of atoms over time. In this context, L_{Min} represents a theoretical minimal lattice spacing that could be achieved if all Ca^{2+} were substituted with Mg^{2+} in hydroxyapatite, while L_{Max} represents the lattice spacing for healthy hydroxyapatite crystals. However, replacing all Ca^{2+} with Mg^{2+} is not attainable in practice. Therefore, we reviewed existing literature to identify suitable values, which were taken as $L_{Min} = 3.403 \text{ \AA}$, $L_{Max} = 3.447 \text{ \AA}$ for the (002) plane and $L_{Min} = 2.243 \text{ \AA}$, $L_{Max} = 2.281 \text{ \AA}$ for the (310) plane [18, 19].

Since the replacement of Ca^{2+} with Mg^{2+} at any time t affects the lattice spacing, we consider that the reduction in lattice spacing occurs at a rate k_7 , which we assume to be proportional to $\frac{dV_{loss}}{dt}$, until L_{Min} is reached. Therefore, our model of crystal lattice spacing change over time must include a term

$$-k_7 \cdot \frac{dV_{loss}}{dt} \cdot (L - L_{Min}).$$

However, if the release of ions becomes negligible over time, the body can remove the incorporated ions and replace them with Ca^{2+} ions instead. In that case, the lattice spacing increases again over time at a rate k_8 until reaching the original lattice spacing L_{Max} . In considering this, the crystal lattice change is affected by the following term:

$$k_8 \cdot (L_{Max} - L).$$

Thus, we overall add two further equations to our ODE system in order to describe the crystal growth and change in lattice spacing over time:

$$\frac{dC_{width}}{dt} = k_4 \cdot C_{width} \cdot \left(k_5 \cdot \frac{dH}{dt}\right)^{k_6} \quad (1f)$$

$$\frac{dL}{dt} = -k_7 \cdot \frac{dV_{loss}}{dt} \cdot (L - L_{Min}) + k_8 \cdot (L_{Max} - L) \quad (1g)$$

with parameters $k_4, k_5, k_6, k_7, k_8 \in \mathbb{R}_{>0}$. L is non-dimensionalized and normalized by $L^* = \frac{L}{L_{max}}$. Similarly, $K^* = \frac{K}{\hat{K}}$, where $\hat{K} = 15 \text{ nm}$ [20], is the non-dimensionalized and normalized description of the crystallite size.

3 Materials and methods

3.1 Experimental data for model calibration

The experimental data used for model calibration in this study stems mainly from animal experiments, in which Ti, Mg-5wt.%Gd and Mg-10wt.%Gd M2 screws have been implanted into the tibia diaphysis of Sprague Dawley rats. The animal experiments were conducted in two separate studies and they were performed after ethical approval by the ethical committee at the Malmö/Lund regional board for animal research, Swedish Board of Agriculture (approval number DNR M 188-15) and at the Molecular Imaging North Competence Centre Kiel (approval number V 241-26850/2017(74-6/17)), respectively. All experimental details have been published in [17, 21, 22]. The animals were sacrificed 4, 8, 10, 12, 20 and 32 weeks after implantation. At that point, the implant and bone surrounding it were explanted and studied using micro computed tomography. Based on the 3D images, which were evaluated at a voxel size of $5 \mu\text{m}$, the implant's volume loss (%) and relative bone volume fraction (%) in its vicinity were computed as described in [21, 22]. Following cutting of thin sections of the

explants, the bone ultrastructure was studied using X-ray diffraction. The crystal lattice spacing and crystallite size along the (310) direction, which is related to the crystal width, were computed for explants obtained after 4, 8 and 12 weeks [17]. Moreover, the crystallite size and crystal lattice spacing along the (002) direction were computed for samples explanted 10, 20 and 32 weeks after implantation [22]. It was shown that the crystallite size along (002), which is related to the length of the crystal, did not differ significantly between time points. Thus, we model a change in crystal width only, but consider the (002) lattice spacing data in modelling.

In a second similar study, Ti pins with a diameter of 1.6 mm and a length of 8 mm produced from Ti6Al7Nb titanium (purchased from Medical University of Graz, Graz, Austria and manufactured by Acnis International, France) were implanted into the femur of Sprague Dawley rats, which were sacrificed after 3, 7, 14, 28 and 90 days. The experiments were performed under ethical approval (Prot. n° 299/2020-PR) by the Istituto Superiore di Sanità on behalf of the Italian Ministry of Health and Ethical Panel. After making an insertion perpendicular to the femur shaft in the mid-diaphysis area. All skin layers were cut through and the femoris muscle tissues were carefully spread apart. After cleaning the bone of the residual soft tissue a hole with a diameter of 1.55 mm was made. The sample was inserted by gentle tapping resulting in a press fit. Then the area was cleaned and the wound was closed. After the different healing times, the animals were sacrificed, and the implants with the surrounding bone were explanted. The bone-implant specimen were embedded in methyl methacrylate by the company LLS Rowiak LaserLabSolutions GmbH (Hanover, Germany). Micro computed tomography experiments were performed at the beamline P05 operated by Helmholtz-Zentrum Hereon at the PETRA III at Deutsches Elektronen Synchrotron (DESY, Hamburg, Germany). The measurements were carried out using a pixel size of 2.56 μm and a resolution of 2.85 μm as determined by a mutual transfer function. Following tomographic reconstruction, the data was segmented using a nnU-net [23] as described in [24], and the relative bone volume fraction (%) in the peri-implant region was computed.

3.2 Model implementation and initial values

The model equations are implemented in Python 3.11 (Spyder, Anaconda) using the ODE-solver *odeint* and the least squares optimization method supplied in *scipy* (v1.14.0) [25].

As initial conditions at $t = 0$, we set $V = 0$, as the implants are assumed to be non-degraded initially. Since equation 1a isn't defined for $t = 0$, we are adding a small error $\varepsilon = 10^{-30}$ to t to be able to solve the equation. We assume that $x_1 = 1$ since all matrix present is initially in its immature state and its production occurred sufficiently fast to be negligible to the model [26]. Therefore $x_2 = 0$. In accordance with Komarova et al., we assume that $I = 1$ and with no nucleators or mineralized bone present $N = 0$ [8]. Consequently, the hydroxyapatite crystal size $K = 0$ at $t = 0$ and we set the initial lattice spacing $L = L_{max}$, assuming an unperturbed crystal lattice. In the absence of data, we assume that $H(t = 0) = 0$. This enables us to still assess the differences between Ti and Mg-xGd implants, since it may be assumed that for similar implantation procedures, such as a press fit, the initial value for H will be similar, and would only need to be offset by a constant. We perform a parameter study and vary the initial value when calibrating to the data from the first study to understand the impact of the initial value. Finally, to assess how well the model holds when $H(t = 0) \gg 0$, we calibrate the model to the experimental data from the second study.

Further, we include a temporal offset t_{lag} as a fitting parameter. This is based on two considerations: firstly, other processes occur in bone following implantation prior and in parallel to bone formation, such as the inflammatory response and angiogenesis. Initial bone formation during intramembraneous healing is visible around 7 days [27], which may be formalized by defining the right hand sides of equations 1a-1f as functions of $t - t_{lag}$ instead of t . This offset is not included in equations 1f and 1g, since they are an averaged representation of crystal width and lattice spacing for any crystal that is formed, irrespective of how much bone has formed. The second consideration for including an offset is based on the fact that bone mineralization starts between 5-10 days after matrix deposition [28], therefore, we may include an artificial data point in our calibration data

for BV/TV at time t_{lag} with $H(t_{lag}) = 0.01$. We implement both strategies to include t_{lag} for comparison.

The model calibration of V_{loss} , $H \propto BV/TV$, C_{width} and L is performed with respect to the median values from experiments. Table 1 contains the tested parameter ranges assessed for the different equations and respective variables and parameters. For calibration, we assume that the bone growth around Ti and Mg-based implants is generally similar, and that the main difference lies in the inhibition effect from the released ions. Therefore, we first calibrate all parameters for equations 1a-g to the data of the Ti screws, but set $m_2 = 0$. We then calibrate the only m_2 and k_3 - k_8 to fit the equations to the data of Mg-10Gd screws. Finally, the same parameters are applied to the different degradation dynamics modelled for Mg-5Gd to assess the validity of the model. The parameters relating to the implant's volume loss are calibrated only in the case of Mg implants. We employ multi-objective least squares optimization to simultaneously fit the parameters of equation 1f and 1e. This approach has several benefits: it allows us to account for the interdependencies between the ODEs, enhances the overall accuracy of the parameter estimation and therefore provides a more comprehensive understanding of the system. $k_2 = 1$ was set for calibration to all materials based on the assumption that only one nucleator is present in the gap between collagen fibres. The Hill function coefficients were set to those values determined by Komarova et al., i.e. $a = 10, b = 0.001$. The order of crystal growth is $k_6 \geq 1$, with values of k_6 generally ranging between 1 and 2 [29] and experimental data indicating a parabolic dependence of hydroxyapatite precipitation on relative supersaturation [30].

Equation	Parameter	Test parameter range	Physical meaning
1 α	m_1	[0, 1]	Scaled diffusion coefficient
1 β	r'	[0, 2]	Surface corrosion rate*
1 β	d'	[0, 2]	Fraction of corroded and precipitated material*
1a,1b	k_1	[0.001, 2]	Rate of collagen matrix maturation
1c	v_1	[0.001, 1]	Rate of inhibitor production
1c	r_1	[0.001, 1]	Rate of inhibitor removal
1c	m_2	[0.001, 300]	Effective rate of inhibition due to Mg degradation
1d	r_2	[15, 30]	Rate of encapsulation of nucleators
1e	k_3	Ti: [0.001, 5], Mg: [0.001, 1000]	Bone growth rate
1f	k_4	Ti: [0.001, 5], Mg: [0.001, 1000]	Proportionality constant between crystal width and surface area
1f	k_5	Ti: [0.001, 5], Mg: [0.001, 1000]	Hydroxyapatite precipitation rate
1f	k_6	Ti: [1, 5], Mg: [1, 3]	Order of precipitation process
1g	k_7	[0, 100]	Rate of Ca^{2+} ion substitution
1h	k_8	[0, 100]	Rate of Mg^{2+} ion removal from crystal
1a-1e	t_{lag}	[5,10]	Delay in bone formation

Table 1: Model parameters and the parameter ranges tested for calibration. *corrected for the implant's initial surface area and volume.

Following optimization, the quality of the fit is determined using the mean absolute error (MAE) and the normalized root mean square error (NRMSE) computed based on all available data points. Moreover, for each model prediction we calculate the 95 % confidence interval by determining the model estimate at each time point and adding and subtracting the margin of error MOE . The margin of error was computed using the standard error of the model estimate and the critical value from the standard normal distribution corresponding to a 95 % confidence level [31]:

$$MOE = 1.96 \times \frac{\sigma}{\sqrt{n}},$$

σ is the standard deviation of the model residuals, n is the sample size (number of time points, at which experimental data is available) and 1.96 is the t-score for a 95 % confidence level.

4 Results and Discussion

4.1 Modelling Mg alloy degradation

Figure 1 shows the calibrated models for equations 1α and 1β for the experimental data of Mg-5Gd and Mg-10Gd implants in study 1. It is visually apparent that the model presented by Gießgen et al. [10] captures the degradation dynamics more closely, while the power law model presented in [9] overestimates the volume loss for later time points. There is no visual difference between Mg-5Gd and Mg-10Gd as modelled by equation 1α , while equation 1β indicates a different trend with higher initial volume losses for Mg-5Gd which level off more strongly over time. These trends agree with the published statistical analysis, which found no significant differences between the materials [21, 22]. However, *in vitro* results had indicated that Mg-5Gd might degrade faster than Mg-10Gd at early time points [32], which would be supported by model 1β .

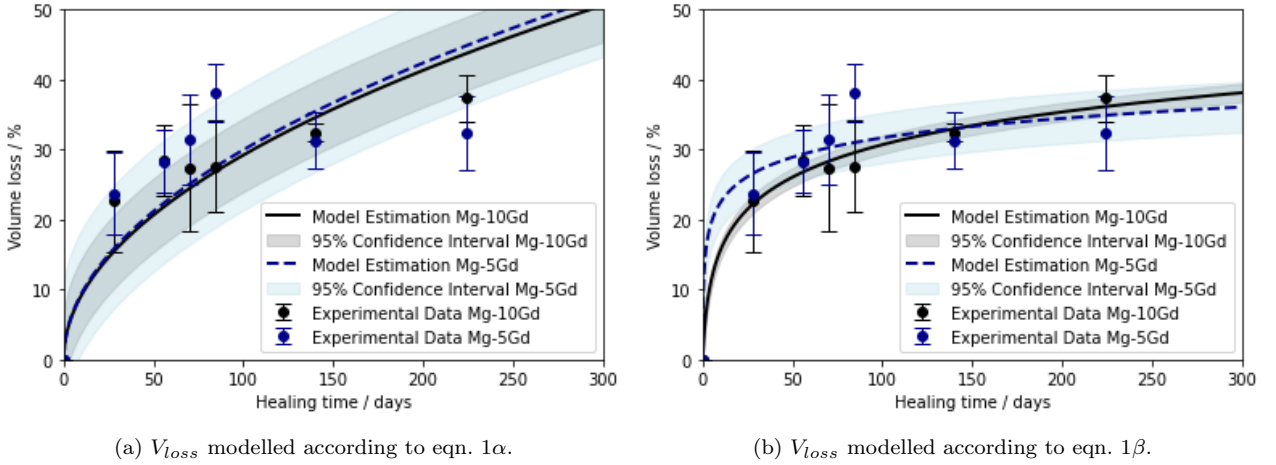


Figure 1: Volume loss of Mg-5Gd (blue dashed line) and Mg-10Gd (black solid line) screws modelled according to eqns. 1α (a) and 1β (b), respectively. The experimental data was taken from [21, 22] and is displayed as median and standard deviation. The model confidence intervals are indicated by transparent areas.

In accordance with the visual impression, the MAEs determined for model 1α are 7.90 % for Mg-5Gd and 4.35 % for Mg-10Gd, while that of model 1β are 2.76 % for Mg-5Gd and 1.12 % for Mg-10Gd. The NRMSE values for all predictions are reported in table 4 in and commented only when providing additional information to the MAE. The calibrated model parameters are given in table 2. These highlight the incapability of the power law to account for the difference in degradation dynamics displayed by Mg-5Gd and Mg-10Gd.

Equation	Parameter	Mg-5Gd	Mg-10Gd
1α	m_1	0.015	0.015
1β	r'	1.104	0.062
1β	d'	0.040	0.068

Table 2: Parameter values for models describing the volume loss calibrated to experimental data.

4.2 Modelling bone growth

Because of the lower errors of model 1β for simulating the volume loss, we will report the corresponding results for the modelled bone growth with respect to this model in the following. For comparison, the results when modelling volume loss using equation 1α is shown in appendix C. Figure 2 shows the fitted *BVTV* model for Ti, Mg-5Gd and Mg-10Gd implants when using the implementation of t_{lag} , where the right hand side of equations 1a-1f is a function of $t - t_{lag}$. The alternative implementation is presented in subsection 4.3.1.

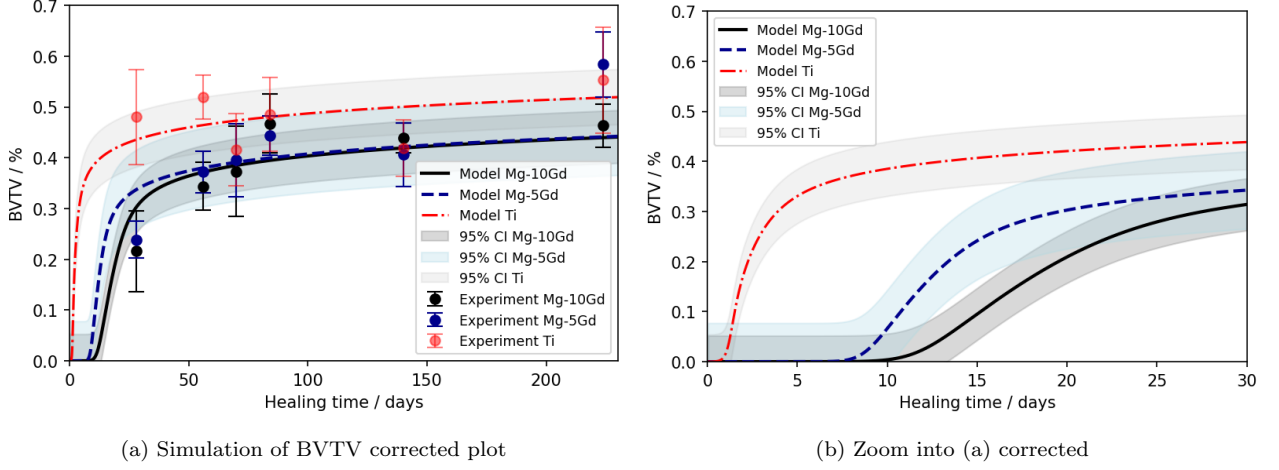


Figure 2: Simulated $BVTV$ according to equation 1e for Ti (red, dotted line), Mg-5Gd (blue, dashed line) and Mg-10Gd (black, solid line) implants. (a) shows the simulation results and experimental data over the course of 230 days, (b) is a zoom into the early time points. The experimental data was taken from [21, 22] and is displayed as median and standard deviation. The model confidence intervals are indicated by transparent areas.

The calibrated model parameters for both bone growth and mineralization are given in table 3.

Equation	Parameter	Ti	Mg-10Gd
1a,1b	k_1	1.4434	-
1c	v_1	0.0010	-
1c	r_1	0.8334	-
1c	m_2	-	138.4876
1d	r_2	26.6094	-
1e	k_3	3.1836	22.4613
1a-1f	t_{lag}	9.6258	-
1f	k_4	3.9601	67.3870
1f	k_5	3.9976	0.7420
1f	k_6	1.0909	1.2515
1g (310)	k_7	-	6.2620
1g (310)	k_8	-	0.0109
1g (002)	k_7	-	2.3037
1g (002)	k_8	-	0.0092

Table 3: Parameter values for equations 1a-1g after calibration to the experimental data. If no value is shown for Mg-10Gd, the value determined for Ti was set.

The MAE determined for the calibrated models shown in Figure 2 is 4.63% for Ti, 4.05% for Mg-10Gd and 5.22% for Mg-5Gd and confirms the visually apparent quality of the model fits. Importantly, this MAE is well below the variance present in the experimental data, highlighting the quality of the calibration. Moreover, the low error for Mg-5Gd shows the predictive power of the models, as no parameters were fitted in this case, except for those describing V_{loss} .

When considering Figure 2(b), it is apparent that the delay in the formation of bone depends on the implant material. In the case of Ti implants, the offset t_{lag} was quantified to be around 9.6 days, which agrees with the literature [27]. The additional delay in bone formation for Mg-based implants relates to the influence of implant degradation. For the given models, based on equation 1 β , this delay is higher for Mg-10Gd implants. This appears counter-intuitive, since a higher degradation rate would be associated with a higher release of ions which would hinder the mineralization, and bears further investigation.

Considering the dynamics of inhibitor concentration in figure 3, it is apparent that I was indeed highest for Mg-5Gd, until approx. 5 days. For both Mg implants, the inhibitor concentration was significantly higher

than for Ti. Similarly, the nucleator concentration was higher for Mg-based implants, and decreased last for Mg-10Gd. The sustained high nucleator concentration can be explained by the high inhibitor concentration, resulting from our implementation where Mg acts as an inhibitor. This high inhibitor concentration prevents the mineralization of the nucleators. In our model, nucleators are only counted when they are not mineralized; once mineralization occurs, nucleator concentration decreases. Our Hill function is designed in such a way that mineralization only initiates when the inhibitor concentration is sufficiently low, leading to a high nucleator concentration as long as the inhibitor concentration remains high. Thus, because the inhibitor concentration degrades faster for Mg-5Gd than Mg-10Gd, bone formation is delayed for the latter.

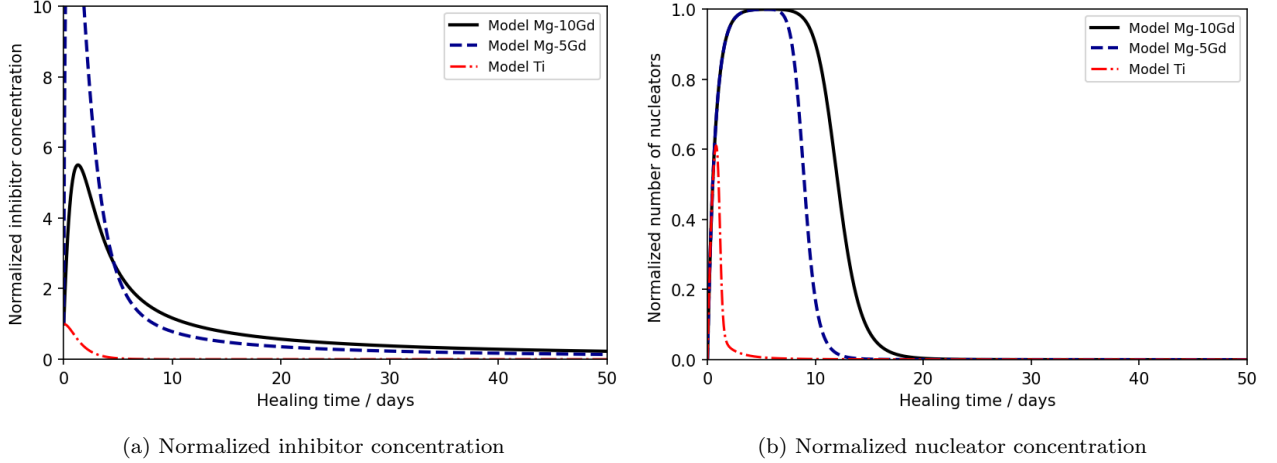


Figure 3: Model output for (a) the normalized inhibitor concentration I computed according to equation 1c and (b) for the normalized nuclear concentration N according to equation 1d for Ti (red, dotted line), Mg-5Gd (blue, dashed line) and Mg-10Gd (black, solid line) implants.

4.3 Modelling changes in hydroxyapatite

The changes in hydroxyapatite crystal width and lattice spacing according to equations 1f and 1g and calibration of the models to the data from study 1 are shown in Figure 4.

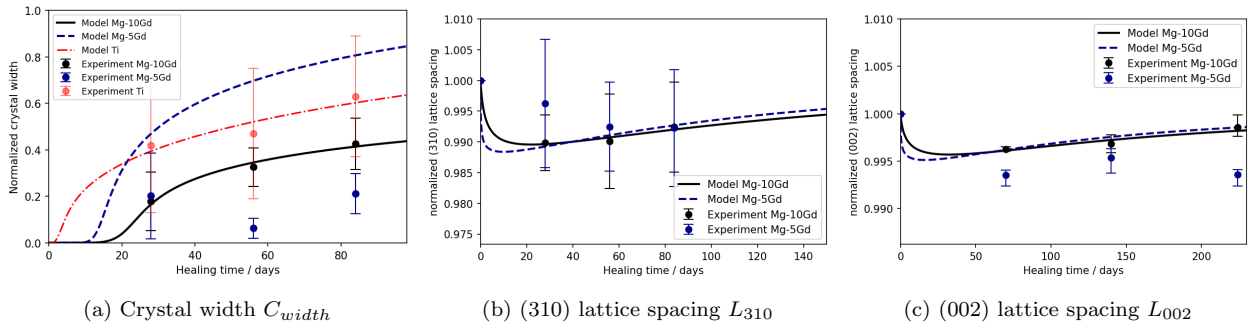


Figure 4: Model output for (a) the normalized crystal width C_{width} computed according to equation 1f for Ti (red, dotted line) Mg-10Gd (black, solid line), and Mg-5Gd (blue, dashed line) implants and (b) for the normalized (310) and (c) the normalized (002) lattice spacing L according to equation 1g for Mg-based implants. The experimental data in (b) is taken from [17], where it was given in mean \pm standard deviation, while that in (c) is taken from [22], which was given as median \pm the 25/75th-percentile.

The resulting MAEs for the computed crystal width were 3.43 % for Ti, 1.48 % for Mg-10Gd and 49.77 % for Mg-5Gd, respectively. Similarly, and visually, the crystal width appears well calibrated for data of Ti and Mg-10Gd implants. Clearly, the fit for Mg-5Gd does not follow the data dynamics. This misfit is related to the high upper bound of k_3 , which, if lowered to values below 10, will result in a fit of C_{width} for Mg-5Gd closer

to Mg-10Gd (not shown). Thus, we may need to consider deriving bounds based on physical meaning in the future. The fitted order of crystal growth k_6 is 1.09 and 1.25, respectively, which agrees with the literature [29].

The prediction of the lattice spacings as displayed in Figure 4(b)-(c), shows that the equation 1g can be well calibrated to predict the change in lattice spacing for Mg-10Gd. When applying the fitted parameters for Mg-5Gd, however, the prediction appears less favourable. While the model fit is still within the reported standard deviation for L_{310} , this is not the case for L_{002} . The MAE for L_{310} was computed as 0.0004 for Mg-10Gd and 0.0029 for Mg-5Gd, respectively. Similarly the MAE for L_{002} was 0.0003 for Mg-10Gd and 0.0032 for Mg-5Gd, respectively. Due to the low absolute values of the lattice spacing the low MAEs may be misleading. The NRMSE reported in table 4 highlights the fact that for L_{002} in particular, the prediction of the model for Mg-5Gd is poor. This may partially be related to the data quality as standard deviations for the (310) reflection are very high. Similarly, the (002) data follows no observable trend and is significantly lower for Mg-5Gd than Mg-10Gd. It is possible, however, that parameters k_7 and k_8 are material specific since, e.g., k_8 effectively describes the removal of Mg^{2+} ions from the bone crystal based on diffusive processes, and must therefore be calibrated for each material individually. In doing so, see appendix D, the dynamics of crystal lattice change over time can be fitted for Mg-5Gd as well. Consequently, the model equation 1g appears well suited to describe the change in lattice spacing due the incorporation of Mg^{2+} ions.

Variable	Ti	Mg-5Gd	Mg-10Gd
$V_{loss} 1\alpha$	-	0.58	0.34
$V_{loss} 1\beta$	-	0.24	0.09
$BVTV$	0.38	3.52	0.20
C_{width}	0.17	0.21	0.06
L_{310}	-	1.04	0.18
L_{002}	-	1.90	0.14

Table 4: NRMSE values of predictions

4.3.1 Alternative implementation of delay

Figure 5 displays the results for $BVTV$ and C_{width} when using the alternative implementation of t_{lag} by introducing $H(t_{lag}) = 0.01$. Visibly, there is little difference in fits for $BVTV$, which is also represented by the computed error metrics (MAE/NRMSE), which are similar for Ti (4.64 %/0.38) but slightly lower for Mg-10Gd (3.89 %/0.19) and Mg-5Gd (4.61 %/0.12). However, when considering the fits for C_{width} these are similar for Ti (3.42 %/0.17) but higher for Mg-10Gd (1.98%/0.08). And once the parameters calibrated for Mg-10Gd are applied for Mg-5Gd the error becomes even larger (69.31 %/4.81) than in the previous implementation. When considering the fitted parameters, which are displayed in Table 5, the similarity for both t_{lag} implementations for Ti is apparent based on the similarity in optimal parameters. Specifically, k_4 - k_6 differ little. However, both parameters m_2 and k_3 are higher in the implementation, where an artificial data point is introduced. Consequently, the enforced longer delay the $BVTV$ for Mg alloys, which results in better fits thereof, appears to result in a worse behaviour of C_{width} . Therefore, with the limited set of experimental data available it appears that the previous implementation of t_{lag} is preferable. However, upon availability of more data, the methodology should be reviewed again.

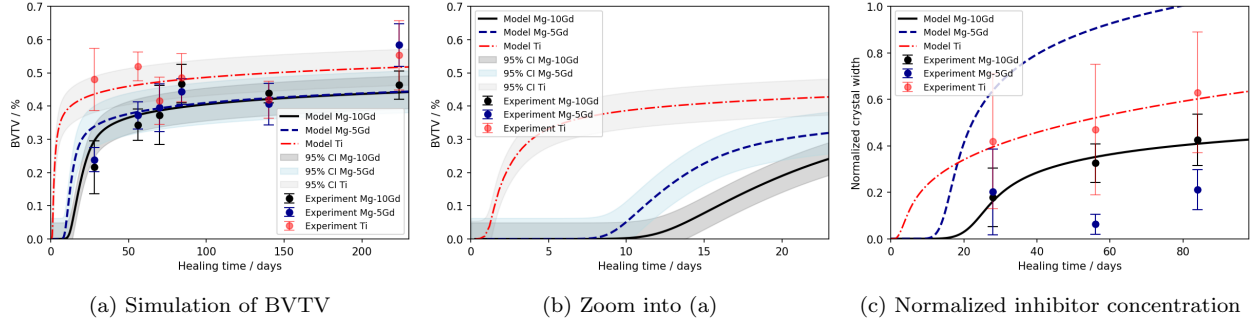


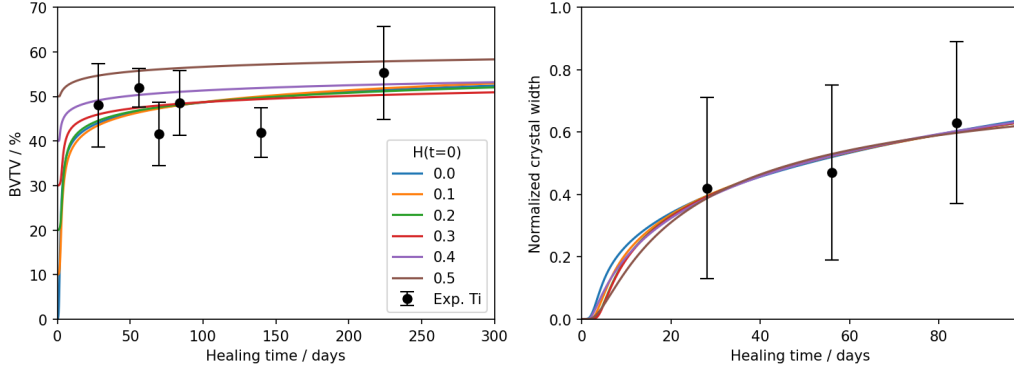
Figure 5: Simulated BVTV according to equation 1e for Ti (red, dotted line), Mg-5Gd (blue, dashed line) and Mg-10Gd (black, solid line) implants. (a) shows the simulation results and experimental data over the course of 230 days. The experimental data was taken from [21, 22] and is displayed as median and standard deviation. (b) shows a zoom into (a). (c) displays the change in crystal width according to equation 1f with experimental data taken from [17].

Equation	Parameter	Ti	Mg-10Gd
1a,1b	k_1	1.4098	-
1c	v_1	0.0014	-
1c	r_1	0.8322	-
1c	m_2	-	149.9449
1d	r_2	27.3117	-
1e	k_3	3.2599	31.3201
-	t_{lag}	5.6259	-
1f	k_4	3.9497	67.0164
1f	k_5	3.9880	0.9839
1f	k_6	1.0876	1.3309

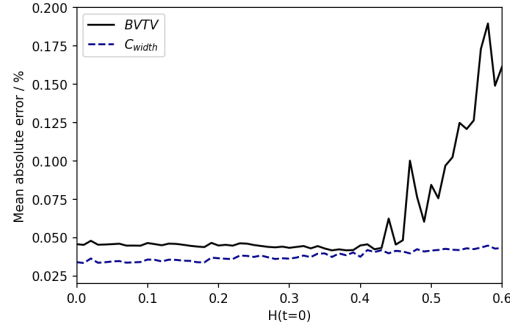
Table 5: Parameter values for equations 1a-1f after calibration to the experimental data. If no value is shown for Mg-10Gd, the value determined for Ti was set.

4.3.2 Dependence on initial value of H

To determine the influence of the initial value for H in the absence of data for $BVTV$ at early time points, we have conducted a parameter study. The results are shown in Figure 6. For $H(t=0) \in [0, 0.42]$, there is little change in the computed MAE for $BVTV$, due to the lack of experimental data at early time points. The MAE of the predicted C_{width} similarly varies little but increases steadily. When considering the prediction, it is apparent that a change in $H(t=0)$ has little effect on the prediction outcome. Therefore, we may conclude that the assumption of an $H(t=0) = 0$ is acceptable in calibrating our model to the data from study 1. We must acknowledge, however, that any interpretation of model variables, such as I and N may be strongly influenced by this lack of data and knowledge.



(a) Fitted model curves for $BVTV$ and C_{width} depending on different $H(t = 0)$.



(b) MAE as a function of $H(t = 0)$ for calibration to Ti data from study 1.

Figure 6: Results of the parameter study for different $H(t = 0)$ and calibration to the Ti data of study 1. (a) shows the resulting fitted curves for $BVTV$ and C_{width} for a number of initial values and (b) displays the respective MAEs as a function of the initial value.

By contrast, earlier time points were investigated in study 2, including a 3-day time point. As indicated by the computed lag time in study 1 and the literature, no new bone growth would have appeared until this point, therefore, the median of the experimental data at this time was set as the initial value for H . Figure 7 shows the resulting fitted curve after calibrating the same parameters as in study 1 for the case of Ti. The computed MAE was 0.007%. The quality of this fit highlights the suitability of the presented model to simulate peri-implant bone growth.

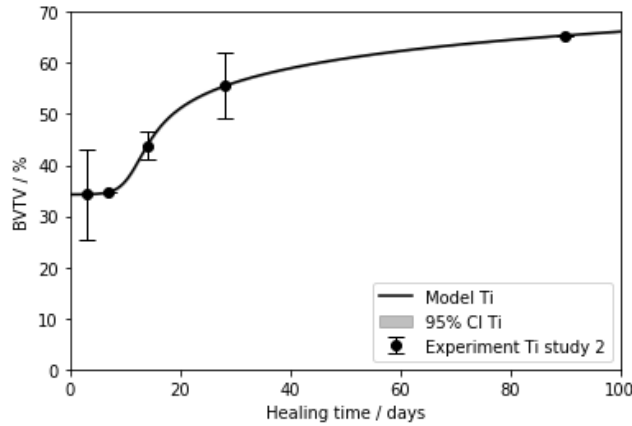


Figure 7: Simulated BVTV according to equation 1e for Ti pins from study 2. The experimental data is displayed as median and standard deviation.

5 Conclusion and outlook

By expanding and refining suitable existing mathematical models of bone growth and implant degradation, we are able to simulate implant degradation and osseointegration at micro- and ultrastructural level for Ti, Mg-10Gd and Mg-5Gd implants. Importantly, the predictive power of the models in modelling relative bone volume fraction is shown and we prove that the mid-term osseointegration response can be predicted well despite lacking data from early time points. Further testing of the model to simulate the response of the bone ultrastructure to biodegradable implants should be conducted in the future, to ensure the model's generalizability.

Acknowledgements

The authors acknowledge funding from the German Ministry for Education and Research (OPTI-TRIALS - 16DKWN112C) and the NextGenerationEU program. We further would like to thank the DFG (Project number 526239533) for financial support. This research was supported in part through the Maxwell computational resources operated at Deutsches Elektronen-Synchrotron, Hamburg, Germany. The authors thank Hanna Ówieka and Kamila Iskhakova for their experimental work which provided data for model calibration in this work.

Data availability

The data sets generated and analyzed during the current study are available from the corresponding authors on reasonable request.

References

1. Tsakiris, V., Tardei, C. & Clicinschi, F. M. Biodegradable Mg alloys for orthopedic implants – A review. *Journal of Magnesium and Alloys* **9**, 1884–1905. ISSN: 2213-9567. <https://www.sciencedirect.com/science/article/pii/S2213956721001699> (2021).
2. He, M., Chen, L., Yin, M., Xu, S. & Liang, Z. Review on magnesium and magnesium-based alloys as biomaterials for bone immobilization. *Journal of Materials Research and Technology* **23**, 4396–4419. ISSN: 2238-7854. <https://www.sciencedirect.com/science/article/pii/S2238785423002557> (2023).
3. Borgiani, E., Duda, G. N. & Checa, S. Multiscale Modeling of Bone Healing: Toward a Systems Biology Approach. *Frontiers in Physiology* **8**. ISSN: 1664-042X. <https://www.frontiersin.org/journals/physiology/articles/10.3389/fphys.2017.00287> (2017).
4. Carlier, A., Geris, L., Lammens, J. & Van Oosterwyck, H. Bringing computational models of bone regeneration to the clinic. *WIREs Systems Biology and Medicine* **7**, 183–194. eprint: <https://wires.onlinelibrary.wiley.com/doi/pdf/10.1002/wsbm.1299>. <https://wires.onlinelibrary.wiley.com/doi/abs/10.1002/wsbm.1299> (2015).
5. Wang, M., Yang, N. & Wang, X. A review of computational models of bone fracture healing. *Med Biol Eng Comput* **55**, 1895–1914 (2017).
6. Ait Oumghar, I., Barkaoui, A. & Chabrand, P. Toward a Mathematical Modeling of Diseases' Impact on Bone Remodeling: Technical Review. *Frontiers in Bioengineering and Biotechnology* **8**. ISSN: 2296-4185. <https://www.frontiersin.org/journals/bioengineering-and-biotechnology/articles/10.3389/fbioe.2020.584198> (2020).
7. Albaraghteh, T., Willumeit, R. & Zeller-Plumhoff, B. In silico studies of magnesium-based implants: A review of the current stage and challenges. *Journal of Magnesium and Alloys* **10** (Nov. 2022).

8. Komarova, S. V., Safranek, L., Gopalakrishnan, J., Ou, M.-j. Y., Mckee, M. D., Murshed, M., Rauch, F. & Zuhr, E. Mathematical model for bone mineralization. *Frontiers in Cell and Developmental Biology* **3**. ISSN: 2296-634X. <https://www.frontiersin.org/journals/cell-and-developmental-biology/articles/10.3389/fcell.2015.00051> (2015).
9. Grogan, J., Leen, S. & McHugh, P. A physical corrosion model for bioabsorbable metal stents. *Acta Biomaterialia* **10**, 2313–2322. ISSN: 1742-7061. <https://www.sciencedirect.com/science/article/pii/S1742706114000038> (2014).
10. Gießgen, T., Mittelbach, A., Höche, D., Zheludkevich, M. & Kainer, K. U. Enhanced predictive corrosion modeling with implicit corrosion products. *Materials and Corrosion* **70**, 2247–2255. eprint: <https://onlinelibrary.wiley.com/doi/pdf/10.1002/maco.201911101>. <https://onlinelibrary.wiley.com/doi/abs/10.1002/maco.201911101> (2019).
11. Ding, H., Pan, H., Xu, X. & Tang, R. Toward a Detailed Understanding of Magnesium Ions on Hydroxyapatite Crystallization Inhibition. *Crystal Growth & Design* **14**, 763–769. eprint: <https://doi.org/10.1021/cg401619s>. <https://doi.org/10.1021/cg401619s> (2014).
12. Iskhakova, K., Wieland, D. C. F., Marek, R., Schwarze, U. Y., Davydok, A., Cwieka, H., AlBaraghteh, T., Reimers, J., Hindenlang, B., Sefa, S., Marinho, A. L., Willumeit-Römer, R. & Zeller-Plumhoff, B. Sheep Bone Ultrastructure Analyses Reveal Differences in Bone Maturation around Mg-Based and Ti Implants. *Journal of Functional Biomaterials* **15**. ISSN: 2079-4983. <https://www.mdpi.com/2079-4983/15/7/192> (2024).
13. Fratzl, P., Fratzl-Zelman, N., Klaushofer, K., Vogl, G. & Koller, K. Nucleation and growth of mineral crystals in bone studied by small-angle X-ray scattering. *Calcified Tissue International* **48**, 407–413. <https://doi.org/10.1007/BF02556454> (1991).
14. Xu, Y., Nudelman, F., Eren, E. D., Wirix, M. J. M., Cantaert, B., Nijhuis, W. H., Hermida-Merino, D., Portale, G., Bomans, P. H. H., Ottmann, C., Friedrich, H., Bras, W., Akiva, A., Orgel, J. P. R. O., Meldrum, F. C. & Sommerdijk, N. Intermolecular channels direct crystal orientation in mineralized collagen. *Nature Communications* **11**, 5068. ISSN: 2041-1723. <https://doi.org/10.1038/s41467-020-18846-2> (2020).
15. Lotsari, A., Rajasekharan, A. K., Halvarsson, M. & Andersson, M. Transformation of amorphous calcium phosphate to bone-like apatite. *Nature Communications* **9**, 4170. ISSN: 2041-1723. <https://doi.org/10.1038/s41467-018-06570-x> (2018).
16. Ostapienko, B. I., Lopez, D. & Komarova, S. V. Mathematical modeling of calcium phosphate precipitation in biologically relevant systems: scoping review. *Biomechanics and Modeling in Mechanobiology* **18**, 277–289. ISSN: 1617-7940. <https://doi.org/10.1007/s10237-018-1087-7> (2019).
17. Zeller-Plumhoff, B., Malich, C., Krüger, D., Campbell, G., Wiese, B., Galli, S., Wennerberg, A., Willumeit-Römer, R. & Wieland, D. F. Analysis of the bone ultrastructure around biodegradable Mg-xGd implants using small angle X-ray scattering and X-ray diffraction. *Acta Biomaterialia* **101**, 637–645. ISSN: 1742-7061. <https://www.sciencedirect.com/science/article/pii/S1742706119307809> (2020).
18. Bystrov, V. S., Paramonova, E. V., Avakyan, L. A., Eremina, N. V., Makarova, S. V. & Bulina, N. V. Effect of Magnesium Substitution on Structural Features and Properties of Hydroxyapatite. *Materials* **16**. ISSN: 1996-1944. <https://www.mdpi.com/1996-1944/16/17/5945> (2023).
19. Gayathri, B., Muthukumarasamy, N., Velauthapillai, D., Santhosh, S. & asokan, V. Magnesium incorporated hydroxyapatite nanoparticles: Preparation, characterization, antibacterial and larvicidal activity. *Arabian Journal of Chemistry* **11**, 645–654. ISSN: 1878-5352. <https://www.sciencedirect.com/science/article/pii/S1878535216300648> (2018).

20. In, Y., Amornkitbamrung, U., Hong, M.-H. & Shin, H. On the Crystallization of Hydroxyapatite under Hydrothermal Conditions: Role of Sebacic Acid as an Additive. *ACS Omega* **5**. PMID: 33134681, 27204–27210. eprint: <https://doi.org/10.1021/acsomega.0c03297>. <https://doi.org/10.1021/acsomega.0c03297> (2020).
21. Krüger, D., Galli, S., Zeller-Plumhoff, B., Wieland, D. F., Peruzzi, N., Wiese, B., Heuser, P., Moosmann, J., Wennerberg, A. & Willumeit-Römer, R. High-resolution ex vivo analysis of the degradation and osseointegration of Mg-xGd implant screws in 3D. *Bioactive Materials* **13**, 37–52. ISSN: 2452-199X. <https://www.sciencedirect.com/science/article/pii/S2452199X21005077> (2022).
22. Iskhakova, K., Cwieka, H., Meers, S., Helmholz, H., Davydok, A., Storm, M., Baltruschat, I. M., Galli, S., Pröfrock, D., Will, O., Gerle, M., Damm, T., Sefa, S., He, W., MacRenaris, K., Soujon, M., Beckmann, F., Moosmann, J., O'Hallaran, T., II, R. J. G., Wieland, D. F., Zeller-Plumhoff, B. & Willumeit-Römer, R. Multi-modal investigation of the bone micro- and ultrastructure, and elemental distribution in the presence of Mg-xGd screws at mid-term healing stages. *accepted at Bioactive Materials* (2024).
23. Isensee, F., Jaeger, P. F., Kohl, S. A., Petersen, J. & Maier-Hein, K. H. nnU-Net: a self-configuring method for deep learning-based biomedical image segmentation. *Nature Methods* **18**, 203–211. ISSN: 15487105 (2 Feb. 2021).
24. Marinho, A. L., Kazimi, B., Cwieka, H., Marek, R., Beckmann, F., Willumeit-Römer, R., Moosmann, J. & Zeller-Plumhoff, B. A comparison of deep learning segmentation models for synchrotron radiation based tomograms of biodegradable bone implants. *Frontiers in Physics* **12**, 1257512. ISSN: 2296424X (Jan. 2024).
25. Virtanen, P., Gommers, R., Oliphant, T. E., Haberland, M., Reddy, T., Cournapeau, D., Burovski, E., Peterson, P., Weckesser, W., Bright, J., van der Walt, S. J., Brett, M., Wilson, J., Millman, K. J., Mayorov, N., Nelson, A. R. J., Jones, E., Kern, R., Larson, E., Carey, C. J., Polat, İ., Feng, Y., Moore, E. W., VanderPlas, J., Laxalde, D., Perktold, J., Cimrman, R., Henriksen, I., Quintero, E. A., Harris, C. R., Archibald, A. M., Ribeiro, A. H., Pedregosa, F., van Mulbregt, P., Vijaykumar, A., Bardelli, A. P., Rothberg, A., Hilboll, A., Kloeckner, A., Scopatz, A., Lee, A., Rokem, A., Woods, C. N., Fulton, C., Masson, C., Häggström, C., Fitzgerald, C., Nicholson, D. A., Hagen, D. R., Pasechnik, D. V., Olivetti, E., Martin, E., Wieser, E., Silva, F., Lenders, F., Wilhelm, F., Young, G., Price, G. A., Ingold, G.-L., Allen, G. E., Lee, G. R., Audren, H., Probst, I., Dietrich, J. P., Silterra, J., Webber, J. T., Slavič, J., Nothman, J., Buchner, J., Kulick, J., Schönberger, J. L., de Miranda Cardoso, J. V., Reimer, J., Harrington, J., Rodríguez, J. L. C., Nunez-Iglesias, J., Kuczynski, J., Tritz, K., Thoma, M., Newville, M., Kümmerer, M., Bolingbroke, M., Tartre, M., Pak, M., Smith, N. J., Nowaczyk, N., Shebanov, N., Pavlyk, O., Brodtkorb, P. A., Lee, P., McGibbon, R. T., Feldbauer, R., Lewis, S., Tygier, S., Sievert, S., Vigna, S., Peterson, S., More, S., Pudlik, T., Oshima, T., Pingel, T. J., Robitaille, T. P., Spura, T., Jones, T. R., Cera, T., Leslie, T., Zito, T., Krauss, T., Upadhyay, U., Halchenko, Y. O., Vázquez-Baeza, Y. & SciPy 1.0 Contributors. SciPy 1.0: fundamental algorithms for scientific computing in Python. *Nature Methods* **17**, 261–272. ISSN: 1548-7105. <https://doi.org/10.1038/s41592-019-0686-2> (3 2020).
26. ElHawary, H., Baradaran, A., Abi-Rafeh, J., Vorstenbosch, J., Xu, L. & Efanov, J. Bone Healing and Inflammation: Principles of Fracture and Repair. *Semin Plast Surg.* (2021).
27. Vieira, A. E., Repeke, C. E., Ferreira Junior, S. d. B., Colavite, P. M., Bigueti, C. C., Oliveira, R. C., Oliveira, R. C., Assis, G. F., Taga, R., Trombone, A. P. F. & Garlet, G. P. Intramembranous bone healing process subsequent to tooth extraction in mice: micro-computed tomography, histomorphometric and molecular characterization. *PloS one* **10**, e0128021. ISSN: 1932-6203 (2015).
28. Meunier, P. & Boivin, G. Bone mineral density reflects bone mass but also the degree of mineralization of bone: Therapeutic implications. *Bone* **21**, 373–377. ISSN: 8756-3282. <https://www.sciencedirect.com/science/article/pii/S8756328297001701> (1997).

29. Mullin, J. in *Crystallization (Fourth Edition)* (ed Mullin, J.) Fourth Edition, 216–288 (Butterworth-Heinemann, Oxford, 2001). ISBN: 978-0-7506-4833-2. <https://www.sciencedirect.com/science/article/pii/B9780750648332500085>.
30. Koutsoukos, P. G., Natsi, P. D., Gartaganis, S. P. & Gartaganis, P. S. Biological Mineralization of Hydrophilic Intraocular Lenses. *Crystals* **12**. ISSN: 2073-4352. <https://www.mdpi.com/2073-4352/12/10/1418> (2022).
31. Hazra, A. Using the confidence interval confidently. *Journal of thoracic disease* **9**, 4125 (2017).
32. Krüger, D., Zeller-Plumhoff, B., Wiese, B., Yi, S., Zuber, M., Wieland, D. F., Moosmann, J. & Willumeit-Römer, R. Assessing the microstructure and in vitro degradation behavior of Mg-xGd screw implants using μ CT. *Journal of Magnesium and Alloys* **9**, 2207–2222. ISSN: 2213-9567. <https://www.sciencedirect.com/science/article/pii/S2213956721002097> (2021).
33. Bronstein, I. N. & Semendjajew, K. A. *Taschenbuch der Mathematik (German) [Pocketbook of mathematics]* 416–417. ISBN: 3-87144-492-8 (Harri Deutsch, 1987).
34. Werner, D. in *Einführung in die höhere Analysis (German) [Introduction into higher Analysis]* 149 (Springer Berlin Heidelberg, Berlin, Heidelberg, 2009). ISBN: 978-3-540-79696-1. https://doi.org/10.1007/978-3-540-79696-1_3.
35. W.Prüss, J. & Wilke, M. *Gewöhnliche Differentialgleichungen und dynamische Systeme (German) [Ordinary differential equations and dynamic systems]* (Springer Basel, 2010).

A Mathematical analysis of existence and uniqueness of solutions

When modelling real-life phenomena with ODEs there are several easy sanity checks one can do from a purely mathematical point of view in order to test the viability of the model:

- Does a (mathematical) solution of the ODE-model exist at all? If it does not, but apparently there is a solution in the real-life application, it is likely that the model is essentially flawed.
- Is the (mathematical) solution of the ODE-model unique? If it is not, it is possible that the simulation yield one of the solutions, while the real-life application would need a totally different solution to be treated and discussed. One should at least be careful, if non-uniqueness is an issue, and it is always easier to deal with ODE-models whose solutions are as unique as the real-life application requires.
- Is the solution positive? When measuring physical entities (like volume), a solution giving negative answers likely once again hints at a flawed ODE-model. (But also see the final bullet point for small volumes!)
- How stable is the solution under small perturbations of the initial data? Real-life measurement and numerical approximation are never precise. Therefore mathematical ODE-models should be forgiving to small perturbations of the initial data.

The following mathematical results help investigate these modelling questions.

Existence and uniqueness of solutions

Theorem 1 (Local Picard-Lindelöf theorem [33, pp. 416-417]). *Let $G \subseteq \mathbb{R}^2$, $(t_0, y_0) \in G$, such that for $\varepsilon, \delta > 0$ so that $U := [t_0 - \varepsilon, t_0 + \varepsilon] \times [y_0 - \delta, y_0 + \delta] \subseteq G$ and $f : G \rightarrow \mathbb{R}$ continuous and locally Lipschitz-continuous with respect to the second variable. Let*

$$M := \sup_{(t,y) \in U} |f(t, y)|, \quad \alpha := \min\left\{\varepsilon, \frac{\delta}{M}\right\}$$

Then there exists exactly one solution to the initial value problem $\dot{y} = f(t, y)$, $y(t_0) = y_0$ on the interval $[t_0 - \alpha, t_0 + \alpha]$.

Since all of our differential equations are characterized by using continuous and locally Lipschitz-continuous functions, this theorem tells us that there exist in fact unambiguous functions solving these differential equations for any initial values and times, at least for short time-frames. If we modify (1d) by inserting the needed derivatives and solutions

$$\frac{dN}{dt} = k_2 \frac{dx_2}{dt} - r_2 \frac{dH}{dt} N \rightarrow \frac{dN}{dt} = k_1 k_2 x_1 - r_2 k_3 \left(\frac{b}{b + I^a} \right) N^2$$

this equation becomes solvable. It is theoretically possible to then step by step construct a solution for any time frame by glueing local solutions together (this can also be done for the other ODEs, but it's simply easier and faster to use the next theorem).

Theorem 2 (Global Picard-Lindelöf theorem [34, p. 149, Theorem III.2.5.]). *Let $G = [a, b] \times \mathbb{R}^n$, for $a, b \in \mathbb{R}$, $f : G \rightarrow \mathbb{R}^n$ a continuous function which satisfies global Lipschitz-continuity with respect to its second variable.*

Then for all $(t_0, y_0) \in G$ the initial value problem $\dot{y} = f(t, y)$, $y(t_0) = y_0$ is uniquely solvable on $[a, b]$.

It is fairly easy to show that the functions describing the other ODEs meet the requirements of the Global Picard-Lindelöf theorem, thus we can conclude that there exist explicit unambiguous functions solving these differential equations.

In most cases however, with the exception of (1 α), (1 β), (1a), (1b), these solutions cannot be expressed using elementary functions only. This means we still need to numerically solve ODEs or integrate to evaluate them.

Positivity of solutions

Theorem 3 (Additive Estimation). *Let $T, Y \subseteq \mathbb{R}$ be intervals, let $f_+ : T \rightarrow \mathbb{R}_{>0}$ and $g : T \times Y \rightarrow \mathbb{R}$ be continuous. If there are differentiable solutions y and y_h for the ODEs*

$$\dot{y} = f_+(t) + g(t, y), \quad \dot{y}_h = g(t, y_h)$$

on T , the following applies:

If there exists $s \in T : y(s) > y_h(s)$, then

$$\forall t \in T_{\geq s} : y(t) > y_h(t).$$

Since we cannot easily express solutions to our ODEs, we developed the additive estimation theorem which provides us with lower bound estimations through solutions of the homogeneous equations. Since these are comparably easy to solve and actually provide us with an expressible explicit function for (1c) which stays positive for positive starting values, it automatically becomes clear that our desired solution behaves accordingly. The same can be said about solutions to (1 α), (1 β), (1a), (1b) just by looking at the explicit solutions for the initial value problems (IVPs) $t_0 = 0$ and $V_0, C_1, x_0 \geq 0$:

$$V_{loss}(t) = V_0 + 2m_1 \sqrt{t} \tag{1\alpha}$$

$$V_{loss}(t) = V_0 + d \log\left(\frac{r't + d'}{d'}\right) \tag{1\beta}$$

$$x_1(t) = C_1 e^{-k_1 t} \tag{1a}$$

$$x_2(t) = x_0 + C_1(1 - e^{-k_1 t}) \tag{1b}$$

Theorem 4 (Multiplicative Estimation). *Let $T, Y \subseteq \mathbb{R}$ be intervals, let $f, h : T \rightarrow \mathbb{R}$ be continuous with $\forall t \in T : f(t) > h(t)$ and let $g_+ : T \times Y \rightarrow \mathbb{R}_{>0}$ be continuous. If there are differentiable Solutions y_f, y_h for the*

ODEs

$$\dot{y}_f = f(t) \cdot g_+(t, y_f), \quad \dot{y}_h = h(t) \cdot g_+(t, y_h)$$

on T , the following applies: if there exists $s \in T : y_f(s) > y_h(s)$, then $\forall t \in T_{\geq s} : y_f(t) > y_h(t)$.

This theorem was also developed to be used in tandem with additive estimation and essentially lets us do a lower bound estimation for (1d) with a much simpler equation

$$\frac{dN'}{dt} = r_2 k_3 N'^2.$$

This equation is solvable and provides a positive expressible solution for positive initial values and thus the same can be said about the solution to the original ODE. Since (1e) is mostly characterized by N , a positive solution N already implies, that any solutions y to a positive IVP for (1e) must already be positive. The same result follows analogously for (1f) and (1g), with H and V_{loss} .

Continuous dependency of the solution on initial data

Definition 5 (Continuous Dependency [35, p. 67, Definition 4.1.1.]). Let $G \subseteq \mathbb{R} \times \mathbb{R}^n$ be open, $f : G \rightarrow \mathbb{R}^n, (t, x) \mapsto f(t, x)$ continuous and locally Lipschitz-continuous with respect to the second variable. Let then x be a solution to the IVP $(t_0, x_0) \in G$ and $\dot{x} = f(t, x)$ and $x(t_0) = x_0$ on its maximal interval of existence T . Let $I \subseteq T$ be compact and define

$$\text{graph}_I(x) := \{(t, x(t)) : t \in I\}.$$

x is called **continuously dependent** of (t_0, x_0, f) if for every compact interval $I \subseteq T$ there exists a compact neighborhood $K \subseteq G$ of $\text{graph}_I(x)$, so that the following holds:

For every $\varepsilon > 0$, there exists a $\delta > 0$, so that for any $g \in C(K, \mathbb{R}^n)$ and $(\tau_0, y_0) \in K$ which satisfy

$$|t_0 - \tau_0| < \delta, |x_0 - y_0| < \delta, \sup_{(s,z) \in K} |f(s, z) - g(s, z)| < \delta$$

any solution y which solves the IVP (τ_0, y_0) for $\dot{y} = g(t, y)$ exists on I and

$$\forall t \in I : |x(t) - y(t)| < \varepsilon.$$

Theorem 6 ([35, p. 68, Theorem 4.1.2.]). Let $G \subseteq \mathbb{R} \times \mathbb{R}^n$ be open with $(t_0, x_0) \in G$, $f : G \rightarrow \mathbb{R}^n$ continuous and locally Lipschitz-continuous with respect to its second variable. If x is a unique non-extendable solution to the IVP $\dot{x} = f(t, x)$, x is continuously dependent on (t_0, x_0, f) .

As discussed earlier we can find unique global solutions to every equation for positive IVPs, thus we can construct a globally unambiguous solution X for the whole system. Continuous dependency essentially tells us that we can introduce small errors into the system, through for example different starting values or variables used, and still get similar behavior without extreme fluctuation. Since each equation is characterized by a locally Lipschitz-continuous function, the same holds true for the function f characterizing the whole system. The Lipschitz-constant can be used to estimate this behaviour: For $t \in [t_{min}, t_{max}] \subset \mathbb{R}_{\geq 0}$, $\delta > 0$, $Y := (V, x_1, x_2, I, N, H, C, L) \in \mathbb{R}_{\geq 0}^8$ and any $Y' := (V', x'_1, x'_2, I', N', H', C', L') \in \mathbb{R}_{\geq 0}^8$ so that $\|Y - Y'\|_2 \leq \delta$ it can

be characterized by determining the following constants:

$$\begin{aligned}
K_1 &:= 2k_1 + v_1 + k_2k_3 \\
K_2 &:= r_1(I + \delta) \\
K_3 &:= r_1x_1 + r_2k_3(N + \delta)^2\hat{G} + k_3(N + \delta)\hat{G} + k_3^{k_6}k_4k_5^{k_6}k_6(C + \delta)\hat{G} \\
K_4 &:= r_2k_3(2N + \delta) + k_3 + k_3^{k_6}k_4k_5^{k_6}k_6(C + \delta) \\
K_5 &:= \hat{V}_{loss} \cdot k_7 + k_8
\end{aligned}$$

Where

$$\hat{G} := ab(I + \delta)^{a-1} + \ln(b + (I + \delta)^a) \quad \hat{V}_{loss} := \dot{V}_{loss}(t_{min}) = \begin{cases} \frac{m_1}{\sqrt{t_{min}}}, & \text{for } 1\alpha \\ \frac{r'd'}{r't_{min}+d'}, & \text{for } 1\beta \end{cases}$$

The Lipschitz constant is then defined follows:

$$K_{Lipschitz} := \max\{1, K_1, \dots, K_5\}$$

Evidently, the \hat{V}_{loss} in 1α is not defined at $t_{min} = 0$. This is not ideal since it ties into the fact that when using 1α our system is not locally Lipschitz at $t = 0$. This however is not a problem with the formula in 1β . Thus when using 1β X is already continuously dependent on (t_0, X_0, f) and therefore quite stable under small errors.

B Derivation of surface area

In order to describe the crystal surface area L_{SA} as a function of time, we aim to relate it to the crystal width. We assume that the crystal may be approximated by a prism with regular n -sided base. We set r_i to be the height of the n triangles that form the base of the structure, such that $2r_i = C_{width}(t)$. This holds true because r_i is also the radius of the inner circle of each of these base triangles. Additionally, let h be the height of the prism and a the length of one side of the n -sided base. The surface area L_{SA} is given by:

$$L_{SA} = 2 \cdot B_A + a \cdot h \cdot n = n \cdot a \cdot r_i + a \cdot h \cdot n = n \cdot a \cdot \frac{C_{width}(t)}{2} + a \cdot h \cdot n.$$

Substituting $a = C_{width}(t) \tan\left(\frac{\pi}{n}\right)$, we get:

$$L_{SA} = \frac{1}{2} \cdot n \cdot C_{width}(t)^2 \cdot \tan\left(\frac{\pi}{n}\right) + C_{width}(t) \cdot \tan\left(\frac{\pi}{n}\right) \cdot h \cdot n.$$

We define $k_9 = \frac{1}{2} \cdot n \cdot \tan\left(\frac{\pi}{n}\right)$ and $k_{10} = \tan\left(\frac{\pi}{n}\right) \cdot h \cdot n$, and therefore obtain:

$$L_{SA} = C_{width}(t)^2 \cdot k_9 + C_{width}(t) \cdot k_{10}.$$

Because we assume that the crystal is only growing in width and that we may neglect the growth in length, we remove the contribution of the base faces to the active surface area and obtain the following formula:

$$L_{SA} = k_{10} \cdot C_{width}(t).$$

C Simulation results for bone growth based on equation 1 α

Figure 8 displays $BVTV$, I , N and C_{width} when using equation 1 α to compute V_{loss} . The MAE values for the computed $BVTV$ when utilizing 1 α to calculate V_{loss} are 2.53% for Mg-10Gd and 5.06% for Mg-5Gd, respectively. And the NRMSE values are 0.12 for Mg-10Gd and 0.16 for Mg-5Gd. At the same time the error values for crystal width are 1.25 % (MAE) and 0.05 (NRMSE) for Mg-10Gd and 16.26 % (MAE) and 1.29 (NRMSE) for Mg-5Gd. These overall slightly improved error values when compared to using 1 β for V_{loss} are related to the significant differences in modelled inhibitor, nucleator and crystal growth dynamics. Specifically, k_6 runs into the lower bound and if unbounded would arrive at non-physical values < 1 . Therefore, despite an improved fit, the use of 1 β for V_{loss} remains preferable.

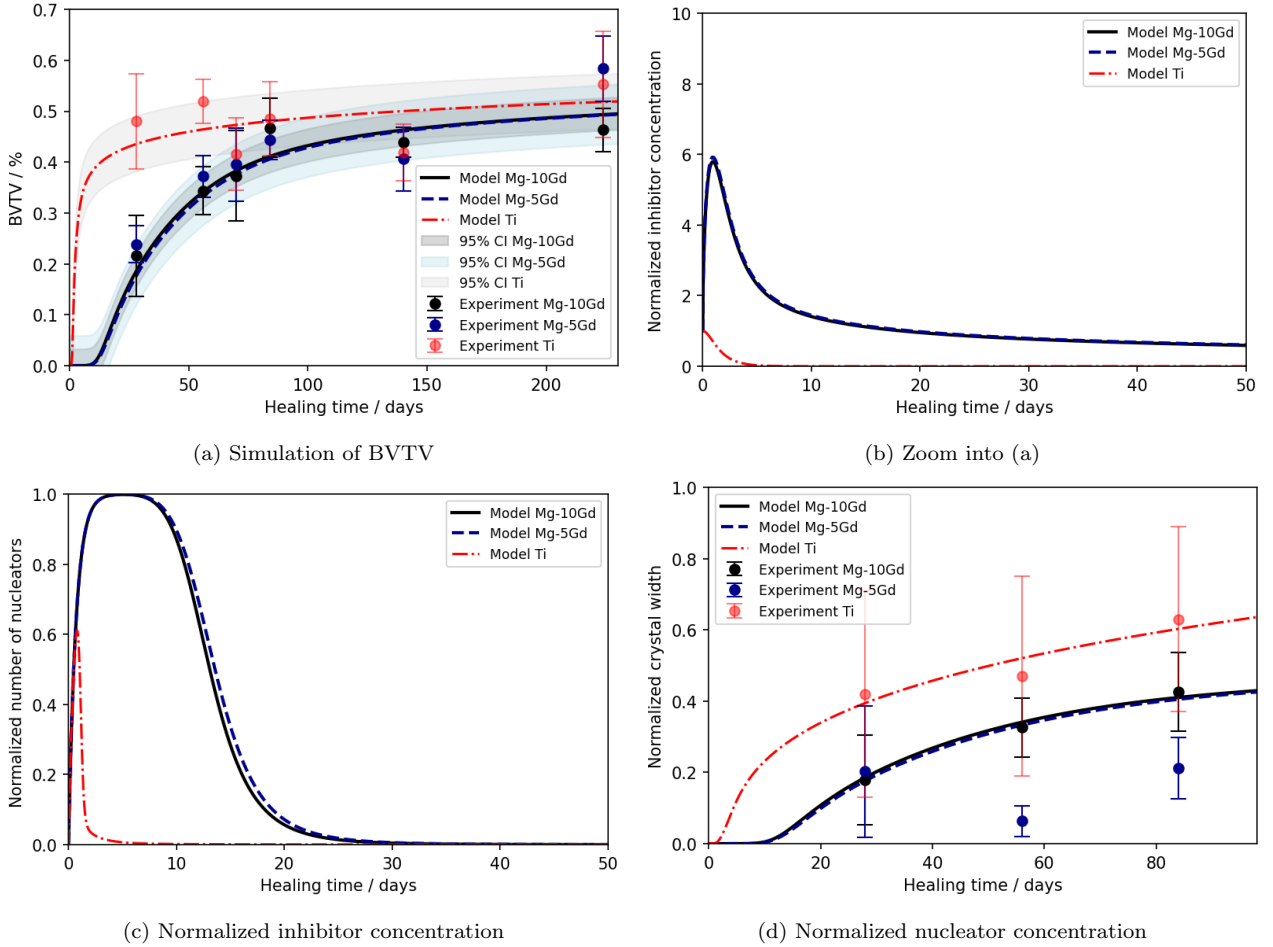
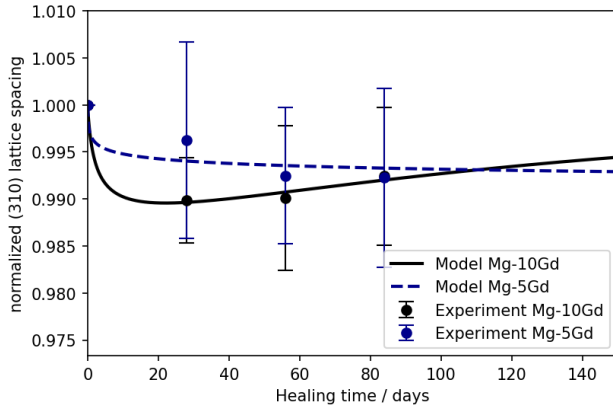


Figure 8: Simulated BVTV according to equation 1e for Ti (red, dotted line), Mg-5Gd (blue, dashed line) and Mg-10Gd (black, solid line) implants. (a) shows the simulation results and experimental data over the course of 230 days. The experimental data was taken from [21, 22] and is displayed as median and standard deviation. (b) shows the model output for the normalized inhibitor concentration I computed according to equation 1c and (c) for the normalized nuclear concentration N . (d) shows the change in crystal width according to equation 1f with experimental data taken from [17].

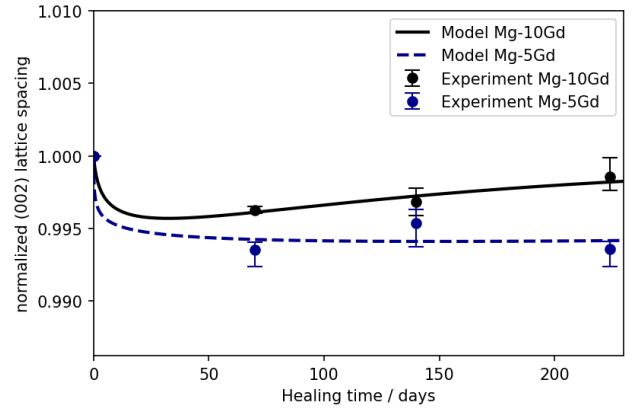
D Material dependent fitting of lattice spacing

Figure 9 displays the fitted lattice spacings and experimental data if the parameters in equation 1g are calibrated individually for both Mg-5Gd and Mg-10Gd. The NRMSE for the Mg-5Gd prediction is lowered by one order of magnitude (0.39 vs. 1.04 for (310) and 0.49 vs. 1.90 for (002)) when an individual fit is found and the MAE improved as well. However, in order to enable the kinetics shown by the data, k_8 decreases by one order of

magnitude for the (002) fit and further to near zero for (310).



(a) (310) lattice spacing L_{310}



(b) (002) lattice spacing L_{002}

Figure 9: Model output for (a) the normalized (310) and (b) the normalized (002) lattice spacing L according to equation 1g for Mg-10Gd (black, solid line), and Mg-5Gd (blue, dashed line) implants. The experimental data in (a) is taken from [17], where it was given in mean \pm standard deviation, while that in (b) is taken from [22], which was given as median \pm the 25/75th-percentile.